Imaging for a Forward Scanning Automotive Synthetic Aperture Radar

SHAHZAD GISHKORI 🔗
University of Edinburgh, Edinburgh, U.K.

LIAM DANIEL 🔗
MARINA GASHINOVA 🔗
University of Birmingham, Birmingham, U.K.

BERNARD MULGREW, Fellow, IEEE
University of Edinburgh, Edinburgh, U.K.

In this paper, we propose a forward scanning synthetic aperture radar methodology for a forward-looking automotive (low-terahertz) radar, which combines scene scanning with synthetic aperture processing, resulting in enhanced angular resolution and improved imaging. We propose two algorithms, first, a modified back-projection (BP) algorithm and, second, a compressed sensing-based BP algorithm. We suggest techniques to reduce computational complexity of the proposed algorithms. Results of simulation and real-data experiments corroborate the validity of our proposed methodology and algorithms.

I. INTRODUCTION

Automotive (Auto-) radar has received a lot of attention over the past few years, especially in the context of advanced driver assistance systems and highly automated driving [1]–[3]. The main role of an Auto-radar in these applications has been restricted to detection and/or collision avoidance only, whereas scene imaging has mostly been performed by optical sensors, e.g., lidar and camera. Imaging capability of the optical sensors is substantially reduced in severe weather conditions, e.g., fog, rain, snow, etc. However, the radar can provide substantial sensing capabilities even in such harsh weather conditions, especially when operating at very high frequencies, and it can create an image of the scene for both ON- and OFF-road driving. Therefore, we are primarily concerned with the imaging scenarios where radar is the only available sensor and all useful information, e.g., detection, classification, height estimation, etc., needs to be extracted from the radar image. Recently, auto-terrain imaging capabilities of a low-terahertz (THz) (150 GHz) radar were presented in [4] by using frequency modulated continuous wave (FMCW) signalling. Low-THz frequencies provide the radar with enhanced penetration capabilities and as a result, the radar can cope with severe weather conditions. However, imaging is limited to short ranges, which is not problematic for auto-driving as the maximum imaging requirement is limited to a fraction of a kilometre only [5]. One major challenge for the Auto-radar imaging is its range and angular resolution (AR), especially when the targets start manoeuvring (e.g., changing lanes, etc.) at short ranges (0.15–30 m) [5], [6]. Range resolution is primarily a function of transmit signal bandwidth, which can be increased to acquire desired results. At low-THz, signal bandwidth is of the order of tens of gigahertz, which can easily provide range resolution of a few centimetres. However, AR is a function of the physical aperture size of the radar antenna. Physical aperture size is generally limited by the physical constraints and cannot be changed arbitrarily. One way to circumvent this problem is to use a synthetic aperture, i.e., the radar illuminates a target scene at multiple locations and the returns are integrated coherently to generate a long synthetic aperture. This functionality gives rise to the term synthetic aperture radar (SAR). Given the movement of the vehicle, SAR processing comes natural to the Auto-radar. Generally, a side looking SAR (SL-SAR), i.e., when the axis of radar view is normal to the axis of radar motion, provides maximum gains of the synthetic aperture. However, a reduction in this normality causes a reduction in the effective synthetic aperture. An Auto-radar, in most part of its functionality, is a forward-looking radar (FL-SAR), i.e., with a high squint angle, instead of a SL radar. This causes a reduction in the effective synthetic aperture. Thus, AR enhancement of an Auto-radar with SAR mechanism has very limited gains. This paper tackles the issue of AR enhancement in this particular scenario.

Prior Works: A lot of work has been done in the past to enhance AR of FL-SAR. In [7], a sector imaging radar for enhanced vision has been presented. It is a bistatic radar

with a single transmit antenna and an array of receive-only antennas. Given the absence of motion between the sensor and the targets, SAR functionality is emulated by sequentially switching between the receive antenna elements in combination with digital beamforming. However, AR is still limited by the length of the receive antenna array. Some direction of arrival-based approaches, e.g., [8]–[10], can also improve AR. However, these approaches generally require *a priori* knowledge of the number of scatterers to be resolved within an antenna beamwidth and/or their performance can be limited by the number of available frequency channels. A large body of literature consists of deconvolution approaches to improve the AR. Since the signal received in the angular domain, for a given range bin, can be considered (under certain assumptions) as a convolution between the antenna pattern and the targets' reflectivity pattern [11], a deconvolution process should improve the AR, in principle. In [12], an iterative noncoherent AR improvement technique has been proposed. Processing is done in the frequency domain by approximating the inverse filter as a geometric series to avoid infinite gain at higher frequencies. However, due to noncoherent processing, the phase information is lost. In [13], a minimum mean square error (MMSE) approach was used to provide adaptive pulse compression resulting in an improved range resolution. The same approach was used in [14] to propose a linear minimum mean square error (LMMSE)-based method for improving AR. The AR is improved in comparison to the matched filter (MF) approach. However, the achieved AR is still comparable to the antenna pattern beamwidth. In [15], a maximum *a posteriori*-based approach has been proposed to improve the AR. A limiting factor for this method is the assumption of Poisson distribution of the targets' reflectivity/scattering. In [16], a truncated singular value decomposition-based approach has been presented to enhance the spatial resolution. This approach was applied to FL-SAR in [17]. However, the key limitation in this approach is the truncation parameter which needs to be learnt.

AR improvement through deconvolution is inherently an ill-posed inverse problem, i.e., the number of unknowns (i.e., angular bins to be resolved) can be much larger than the number of available measurements. This is also referred to as an underdetermined problem. The ill-posed nature of the problem can be circumvented by using certain regularization techniques. This can also result in enhancing certain features of the target scene, e.g., sparsity, grouping of the targets, nonnegative nature of their reflectivities, etc. In general, the problem is formed as a least squares (LS) minimization problem regularized by various constrains. A common regularization technique, with connotations to the Wiener filter, is Tikhonov regularization, which penalizes the LS cost function with an ℓ_2-norm penalty. This can result in a unique solution to the problem. However, this method is devoid of sparsity. Replacing the ℓ_2-norm penalty with an ℓ_1-norm penalty can offer a sparse solution. This observation forms a key component of a recently introduced technique of compressed sensing (CS) [18], [19], as a

solution to the underdetermined problem. CS has been used in the radar related problems in a number of papers, either to create sparsity or to improve resolution (azimuth/range) or to reduce speckle, etc. (see, e.g., [20]–[22] and references therein). In [23], CS was used to improve the AR of a scanning phased array radar. AR improvement is achieved by oversampling the antenna pattern and by solving the resulting underdetermined system by CS. Constraints on the measurement process are satisfied by limiting the number of targets in the scanned scene. In this paper, we use a similar approach to increase AR of an Auto-radar for a given range bin. However, our method includes SAR processing as well, which has the ability to enhance AR even further. In terms of SAR processing, a number of classical algorithms are available, e.g., Doppler beam sharpening, range migration algorithm [11], back-projection (BP) [24], and their variants. Except for BP, most of these techniques have their limitations and can perform only under certain conditions. BP algorithm, on the other hand, is quite flexible and it can accommodate a variety of imaging scenarios. However, a limiting factor for BP algorithm is its computational complexity. Nonetheless, some fast implementations of BP are also available, as explained in subsequent sections.

Our Contributions: In this paper, we provide signal processing techniques to enhance AR of the Auto-radar with the aim of forming a two-dimensional (2D) radar image. We use a monostatic FMCW radar working at low-THz frequencies. The radar scans the target scene at multiple look angles (LAs) and then moves forward to the next scanning position/step over the aperture. We call this process as forward scanning SAR (FS-SAR). Note that steering the radar beam at multiple LAs can be done mechanically as well electronically. For the ease of explanation, we assume here a mechanically steered beam. We develop algorithms for the FS-SAR mode and verify their effectiveness via simulation as well as real-data experiments in controlled laboratory conditions. Note, on-the-road experiments are out of the scope of this paper since the main objective here is to introduce novel techniques to provide AR enhancement for Auto-radar imaging. The salient features of our paper are detailed as follows.

1) We propose an FS-SAR methodology as a new mode of SAR operation. We use Auto-radar as our primary application. However, the FS-SAR methodology can be extended to other FL scenarios.
2) We present a mathematical analysis for the composite antenna pattern generated by FS-SAR. We show that FS-SAR methodology causes an improvement in the effective aperture and an increase in the composite antenna gain. This results in the enhancement of AR.
3) We present two algorithms for the FS-SAR mode, i.e., a modified BP algorithm, and a CS-based BP algorithm. The modified BP algorithm jointly utilizes the radar returns from all the angles and all the aperture positions. This algorithm can work directly on the radar returns and does not necessarily require any preprocessing. The CS-based BP algorithm enhances AR by reconstructing

an individual scan followed by SAR processing over the reconstructed returns of all the scans. This algorithm capitalizes on the sparsity of the scene and it has the ability to reconstruct extended targets in the radar image.

4) We show that the computational complexity of the proposed algorithms is not a bottleneck for their practical implementation and it can be easily managed by using the already available techniques on complexity reduction.

5) We verify our proposed methodology and algorithms via both simulations as well as real-data measurements. We show that our methods can perform better than the existing technique.

Organization: Section II presents the system model, Section III give details on the FS-SAR methodology by using the composite antenna pattern, Section IV describes the proposed algorithms, i.e, modified BP and CS-based BP, along with their computational complexities, Section V demonstrates the effectiveness of the proposed methods via simulation as well as real-data experiments and conclusions are given in Section VI.

Notations: Matrices are in upper case bold, while column vectors are in lower case bold, $[\mathbf{X}]_{i,j}$ is the ijth entry of the matrix $\mathbf{X}$, $\mathbf{I}_N$ is the identity matrix of size $N \times N$, $\mathbf{0}_N$ is a vector of zeros of size $N \times 1$, $(\cdot)^T$ denotes Transpose, $(\cdot)^H$ is Hermitian, $(\cdot)^{-1}$ denotes inverse, $\lfloor \cdot \rfloor$ is the floor function, $\otimes$ stands for the Kronecker product, $\star$ describes the convolution, $\hat{\mathbf{x}}$ is the estimate of $\mathbf{x}$, $\triangleq$ defines an entity, $\mathcal{F}\{\cdot\}$ describes a Fourier transform operation, $\uparrow_{\kappa,\kappa'}(\mathbf{X})$ upsamples the matrix $\mathbf{X}$ by an order κ along its rows and by an order κ' along its columns, $\mathcal{O}(\cdot)$ is the big O notation for complexity, and the ℓ_p-norm of a vector $\mathbf{x}$ is denoted as $||\mathbf{x}||_p = (\sum_{i=0}^{N-1} |[\mathbf{x}]_i|^p)^{1/p}$.

II. SYSTEM MODEL

Traditional SAR has two basic modes of operation, which are as follows:

1) stripmap mode SAR (Strip-SAR), where the radar illuminates a target scene at a fixed LA while moving on along its aperture;

2) spotlight mode SAR (Spot-SAR), where the radar illuminates a fixed target scene from multiple LAs.

Our proposed FS-SAR mode of operation for Auto-SAR has somethings in common with 1) and 2). At each scan step, the radar scans the target scene at different LAs and then moves on to the next scan step over the aperture. However, in our case, neither the target area remains fixed as in Spot-SAR, nor the LA remains fixed as in Strip-SAR. The contrast between standard SAR modes and FS-SAR mode of Auto-SAR generates new opportunities as well as new challenges. Our aim here is to capitalize on the opportunities and tackle the challenges for an improved radar imaging.

The FS-SAR can schematically be represented as in Fig. 1, for 2D processing. It has multiple scan steps, l, along the synthetic aperture, i.e., $l \in [-(L-1)/2, (L-1)/2]$.
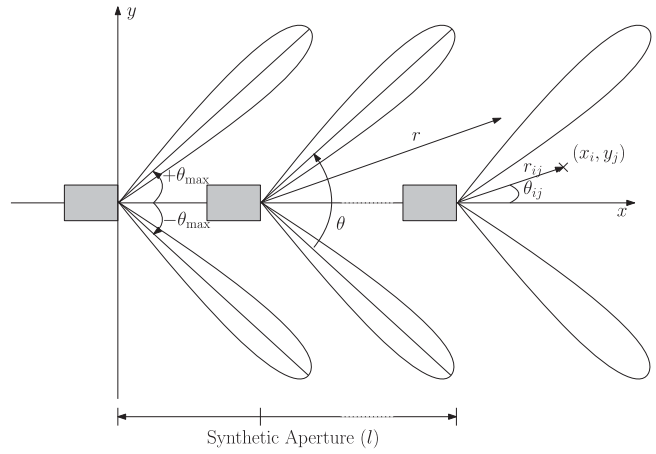

Fig. 1. FS-SAR schematic (2D).

For each scan step, the radar scans at multiple LAs, θ, with angular range, $\theta \in [-\theta_{\max}, +\theta_{\max}]$. The target range, r is the Euclidean distance between the target and the radar with $r \in (0, R_{\max}]$. The target scene is visualized in a Cartesian coordinate system (CCS), i.e., target location is represented as (x_i, y_j) with x_i and y_j being coefficients of x-axis and y-axis, respectively. The target can also be represented in a polar coordinate system, i.e., $r_{ij} \angle \theta_{ij}$, where $r_{ij} \triangleq \sqrt{x_i^2 + y_j^2}$ and $\theta_{ij} \triangleq \arctan(y_j/x_i)$ (w.r.t. the current position of radar). Note, Fig. 1 shows the radar moving along x-axis only. However, it is not a limitation of the proposed method and the radar can undertake any kind of motion in principle.

In our system model, we assume that the radar works on a stop-and-go principle, i.e., the radar is static during the transmission of an FMCW pulse. In general, FMCW pulses are long. Therefore, stop-and-go assumption may not remain valid, as there is a possible motion of the radar platform during the transmit pulse, giving rise to the instantaneous Doppler. A number of methods are available to compensate for such a radar motion, both in the frequency domain, e.g., [25], [26] and in the time domain, e.g., [27]. In our case, our proposed algorithms work in the time domain. Therefore, we can easily use the approach of [27] to compensate for the radar motion during the transmit pulse. This essentially comprises of shifting the pulse contributions by a term which is a function of radar velocity and the squint angle between radar and the target. However, to keep the model simple, in this paper, we continue with the stop-and-go principle. Nonetheless, extensions for instantaneous Doppler compensation are straightforward and they do not affect our proposed approaches.

Let the generic FMCW transmit pulse be of the form

$$s^{\mathrm{Tx}}(t) = \exp\left(j2\pi f_0 t + j\pi\beta t^2\right) \qquad (1)$$

where f_0 is the carrier frequency, $\beta \triangleq B/T$ is the chirp rate defined as the ratio between bandwidth B of the transmitted signal and pulse repetition interval (PRI) T, and t is the fast time variable valid within the PRI, i.e., $0 \le t < T$. We

assume that one such pulse is transmitted at every LA[1], over the complete aperture. The received signal is the sum of reflections from different scatterers within the radar beamwidth. At lth scan step and θth LA, the received signal can be written as

$$s_{l,\theta}^{\text{Rx}}(t) = \sum_{u=1}^{U} \alpha_u \exp\left(j2\pi f_0[t - \tau_{l,\theta}(u)] \right.$$
$$\left. + j\pi\beta[t - \tau_{l,\theta}(u)]^2\right) \quad (2)$$

where α_u is the reflectivity coefficient (which includes the effects of range related variations in the backscattered energy) and $\tau_{l,\theta}(u)$ is the two-way time delay of the uth scatterer. Note that the total number of scatterers U can vary for different scan steps and LAs but we assume them to be the same here for ease of notations. The received signal is mixed with the transmit signal, a process known as deramping, and low-pass filtered, generating an intermediate frequency, also known as beat frequency, corresponding to individual targets. The resulting signal can be written as

$$\tilde{s}_{l,\theta}(t) = \sum_{u=1}^{U} \alpha_u \exp(j2\pi f_0\tau_{l,\theta}(u))$$
$$\exp(j2\pi\beta\tau_{l,\theta}(u)t) \exp\left(-j\pi\beta\tau_{l,\theta}^2(u)\right) \quad (3)$$

where the frequency of the sinusoid $\exp(j2\pi\beta\tau_{l,\theta}(u)t)$ carries information regarding target range, which can be easily observed by doing a Fourier analysis of (3), the exponent $j2\pi f_0\tau_{l,\theta}(u)$ is important for SAR processing because it traces a target over the aperture, and the exponent $j\pi\beta\tau_{l,\theta}(u)^2$ is the unwanted phase term, also known as residual video phase (RVP), which can be removed via a deskewing process. Note, the deskewing process essentially applies a frequency dependent filter in order to remove the RVP, which is proportional to the delay (i.e., range) [28]. Applying deskewing on (3), we can write

$$s_{l,\theta}(t) = \mathcal{F}^{-1}\{\mathcal{F}\{s_{l,\theta}(t)\} \exp(j\pi f^2/\beta)\}$$
$$\approx \sum_{u=1}^{U} \alpha_u \exp(j2\pi f_0\tau_{l,\theta}(u)) \exp(j2\pi\beta\tau_{l,\theta}(u)t) \quad (4)$$

where f is the frequency parameter corresponding to t. The range profile can be generated by taking the Fourier transform of $s_{l,\theta}(t)$ and then using a linear transformation from the frequency domain axis to the range domain axis [24], i.e.,

$$x_{l,\theta}(r) = \mathcal{F}\{s_{l,\theta}(t)\}|_{r=\frac{fc}{2\beta}} \quad (5)$$

where r being the range variable with linear transformation, $r = fc/2\beta$. Sampling the range domain at the Nyquist rate means that the range resolution, Δ_r, can be defined as, $\Delta_r \triangleq c/2B$, and the range bin can be referenced as, r_{n_r}, for $n_r = 0, 1, \ldots, N_r - 1$, where $N_r \triangleq R_{\max}/\Delta_r$. Now, let us focus on scene variations along the azimuth, for a specific range

bin. From (5), we can represent the target scene reflectivities along azimuth for the r_{n_r}th range bin by $x_{l,r_{n_r}}(\theta)$, i.e.,

$$x_{l,r_{n_r}}(\theta) = \{x_{l,\theta}(r_{n_r})\}_{\theta=-\theta_{\max}}^{+\theta_{\max}}. \quad (6)$$

Note, we drop the subscript n_r from $x_{l,r_{n_r}}(\theta)$ in the above-mentioned equation. The received signal along the azimuth can be considered as a convolution between the antenna beam and the target scene reflectivities at a given range bin [11]. If $h(\theta)$ represents the antenna beam of angular length 2ϕ (i.e., the antenna beam pattern is uniformly sampled over $-\phi$ to $+\phi$), then the signal measured along the azimuth, for range r and scan step l, can be written as

$$y_{l,r}(\theta) = h(\theta) \star x_{l,r}(\theta) + n_{l,r}(\theta) \quad (7)$$

where $y_{l,r}(\theta)$ is the measured signal and $n_{l,r}(\theta)$ is the additive white Gaussian noise (AWGN) with element wise variance, σ^2. The AR of a radar is essentially a function of its 3 dB beamwidth, i.e., $\theta_{3\,\text{dB}}$. Let the azimuth domain is sampled at an angular interval, $\delta_\theta = \theta_{3\,\text{dB}}/\zeta$, where ζ is a positive integer and its value depends on the required AR. For very high AR, $\zeta \gg 1$. Then, we can represent $h(\theta)$ as an $N_h \times 1$ vector, $\mathbf{h} \triangleq [h(-\phi), h(-\phi + \delta_\theta), \ldots, h(+\phi)]^H$, where $N_h = \lfloor 2\phi/\delta_\theta \rfloor + 1$. Due to physical limitations, the radar is not able to take measurements at as fine an angular sampling interval as δ_θ. Therefore, let the angular interval for measurements is represented as, $\Delta_\theta = \xi\delta_\theta$, where $\xi \geq 1$. For a very coarse angular measurement interval, $\xi \gg 1$. Then, we can represent $y_{l,r}(\theta)$ as an $N_\theta \times 1$ vector, $\mathbf{y}_{l,r} \triangleq [y_{l,r}(-\theta_{\max}), y_{l,r}(-\theta_{\max} + \Delta_\theta), \ldots, y_{l,r}(+\theta_{\max})]^H$, where $N_\theta = \lfloor 2\theta_{\max}/\Delta_\theta \rfloor + 1$. Similar to $h(\theta)$, $x_{l,r}(\theta)$ can be represented as an $N_x \times 1$ vector, $\mathbf{x}_{l,r} \triangleq [x_{l,r}(-\tilde{\theta}_{\max}), x_{l,r}(-\tilde{\theta}_{\max} + \delta_\theta), \ldots, x_{l,r}(+\tilde{\theta}_{\max})]^H$, where $\tilde{\theta}_{\max} \triangleq \theta_{\max} + (N_h - 1)\delta_\theta/2$ and $N_x = \xi N_\theta + N_h - 1$. Note, by introducing $\tilde{\theta}_{\max}$ in $\mathbf{x}_{l,r}$, we make sure to account for all the contributing targets within the radar beamwidth, for each measurement. Finally, $n_{l,r}(\theta)$ can be represented as an $N_\theta \times 1$ vector, $\mathbf{n}_{l,r} \triangleq [n_{l,r}(-\theta_{\max}), n_{l,r}(-\theta_{\max} + \Delta_\theta), \ldots, n_{l,r}(+\theta_{\max})]^H$. Thus, we can write (7) in the following discrete form:

$$\mathbf{y}_{l,r} = \mathbf{GH}\mathbf{x}_{l,r} + \mathbf{n}_{l,r} \quad (8)$$

where $\mathbf{H}$ is the $(\xi N_\theta - 1) \times N_x$ Toeplitz matrix, defined as

$$\mathbf{H} \triangleq \begin{pmatrix} \mathbf{h}^H & & \mathbf{0}_{(N_x - N_h)}^T \\ 0 & \mathbf{h}^H & \mathbf{0}_{(N_x - N_h - 1)}^T \\ \vdots & \vdots & \vdots \\ \mathbf{0}_{(N_x - N_h)}^T & & \mathbf{h}^H \end{pmatrix} \quad (9)$$

depicts the convolution between the antenna beam pattern and the target scene, and $\mathbf{G}$ is an $N_\theta \times (\xi N_\theta - 1)$ selection matrix, i.e, $[\mathbf{G}]_{n_\theta,:} = [\mathbf{I}_{(\xi N_\theta - 1)}]_{(\xi n_\theta - \xi + 1),:}$, for $n_\theta = 0, 1, \ldots, N_\theta - 1$. Here, we assume $\mathbf{H}$ to be the same for each scan step as well as for each range bin. This assumption has been considered for the sake of simplicity. However, variations in $\mathbf{H}$ with different scanning steps can easily be accommodated in the model. Now, for all range bins, we
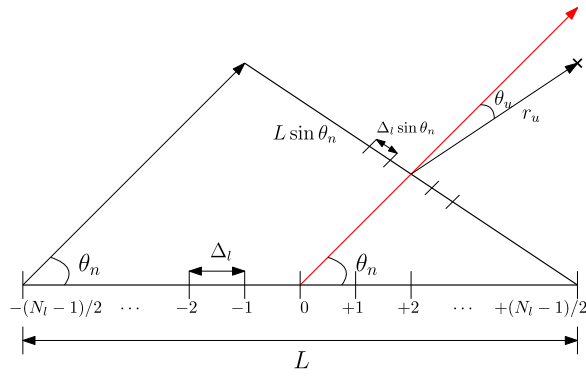

Fig. 2. (FL-)SAR: Synthetic antenna array for LA, θ_n.

can modify (8) as

$$\mathbf{Y}_l = \mathbf{GHX}_l + \mathbf{N}_l \qquad (10)$$

where $\mathbf{Y}_l \triangleq [\mathbf{y}_{l,0}, \mathbf{y}_{l,\Delta_r}, \ldots, \mathbf{y}_{l,(N_r\Delta_r-N_r)}]$, $\mathbf{X}_l \triangleq [\mathbf{x}_{l,0}, \mathbf{x}_{l,\Delta_r}$, $\ldots, \mathbf{x}_{l,(N_r\Delta_r-N_r)}]$, and $\mathbf{N}_l \triangleq [\mathbf{n}_{l,0}, \mathbf{n}_{l,\Delta_r}, \ldots, \mathbf{n}_{l,(N_r\Delta_r-N_r)}]$ are $N_\theta \times N_r$, $N_x \times N_r$ and $N_\theta \times N_r$ matrices, respectively.

III. FS-SAR METHODOLOGY

Our main goal is to use SAR concepts to enhance the AR of an Auto-radar. However, Auto-radar functions as an FL-SAR, most of the times. Therefore, standard SAR can make only limited contributions to the AR enhancement. The FS-SAR methodology increases SAR capabilities by scanning the target scene at multiple LAs over the complete aperture. In this section, we show how FS-SAR method can contribute to the AR enhancement of an Auto-radar by comparing its composite antenna pattern with that of the standard SAR.

A. FL-SAR Antenna Pattern

Conceptually, a synthetic aperture is similar to a phased antenna array, in that each point on the aperture can be considered as an antenna element. However, the difference is that all the elements are not activated at the same time and the output of the synthetic array can be computed by adding the individual contributions of each element. The synthetic aperture comprises of the complete stretch of the synthetic array. This is the case for an SL-SAR, i.e., the LA of the radar is normal to the velocity of radar platform. For the FL-SAR, the LA of the radar is not normal to the velocity of the radar platform. Therefore, effective aperture is reduced and this reduction is proportional to the LA. Fig. 2 shows the schematic of a SAR, where L is the total length of the synthetic aperture with N_l antenna elements of spacing Δ_l, i.e., $L = N_l\Delta_l$. At an LA θ_n, the effective aperture is given as $L \sin\theta_n$ and the element spacing amounts to $\Delta_l \sin\theta_n$. To find the antenna pattern of the synthetic array for the θ_nth LA, let a continuous signal $\exp(j2\pi ft)$ is transmitted from n_lth aperture element, for, $n_l = -(N_l - 1)/2, \ldots, (N_l - 1)/2$. Given a single target scatterer at a distance r_u and angle θ_u from the n_lth aperture element, the composite received signal of the synthetic antenna array can be written
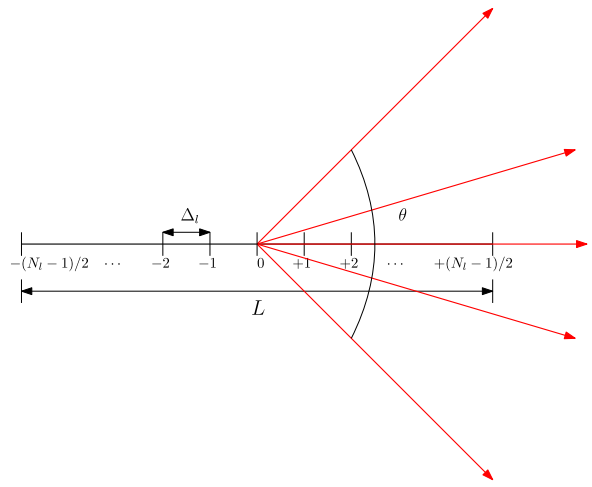

Fig. 3. FS-SAR: Synthetic antenna array, with multiple LAs.

as follows:

$$
\begin{aligned}
s_{\theta_n}(t) &= \sum_{n_l} \exp\{j2\pi f\,(t - 2r_u/c + 2n_l\Delta_l \sin\theta_n \sin\theta_u/c)\} \\
&= C_u \sum_{n_l} \exp\{j2\pi n_l \Delta_l \sin\theta_n \sin\theta_u/\lambda\} \\
&= C_u \frac{\sin\left(2\pi N_l \Delta_l \sin\theta_n \sin\theta_u/\lambda\right)}{N_l \sin\left(2\pi \Delta_l \sin\theta_n \sin\theta_u/\lambda\right)} \\
&\approx C_u \operatorname{sinc}\left(2\pi N_l \Delta_l \sin\theta_n \sin\theta_u/\lambda\right) \qquad (11)
\end{aligned}
$$

where $C_u \triangleq \exp\{j2\pi f(t - 2r_u/c)\}$, and we use the approximation, $\sin(\varphi) \approx \varphi$, for small φ.[2] We can see that (11) generates a symmetric antenna pattern of an FL-SAR. The AR can then be determined by finding the angle at which the sinc function produces a first null. This happens when

$$\sin\theta_u = \frac{\lambda}{2L \sin\theta_n} \qquad (12)$$

and the AR can be calculated as

$$\Delta_{\mathrm{AR}}^{\mathrm{FL-SAR}} = \frac{r_u\lambda}{2L \sin\theta_n}. \qquad (13)$$

From (13), we can see that the effect of synthetic aperture is maximum when radar functions as SL-SAR. However, in case of FL-SAR, effective aperture decreases proportional to the LA, i.e., θ_n.

B. FS-SAR Antenna Pattern

In FS-SAR approach, we scan the target scene at multiple LAs for each aperture element.

Fig. 3 shows the schematic for synthetic array with multiple LAs, parameterized by θ. Following (11), we can write the composite signal received at the synthetic array for

---

[2]Note, this approximation is used for the sake of compact representation only. However, it is not imperative for the validity of the analysis.
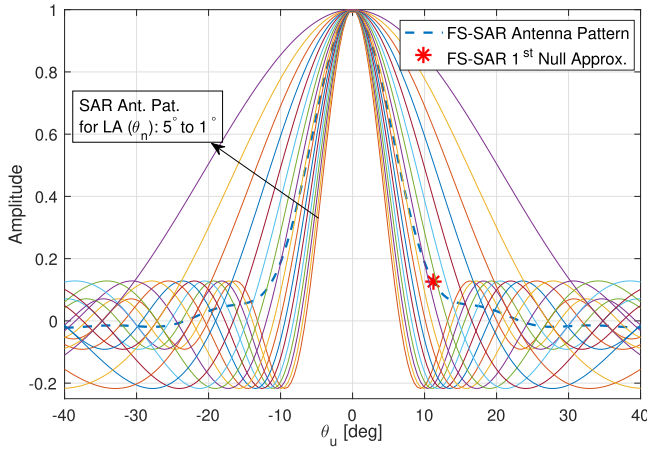
Fig. 4. Composite antenna pattern (Normalized).

Fig. 5. Composite antenna pattern.

multiple LAs θ_n, for $n = -(N_\theta - 1)/2, \ldots, (N_\theta - 1)/2$, as

$$s(t) = \sum_n s_{\theta_n}(t)$$

$$\approx C_u \sum_n \text{sinc} \left(2\pi N_l \Delta_l \sin \theta_n \sin \theta_u / \lambda\right) \quad (14)$$

which also provides the symmetric composite antenna pattern for FS-SAR method. Finding a closed-form solution of (14) is difficult. However, in order to find the Rayleigh beamwidth of the composite antenna pattern, we make an approximation. We can see from (11) that for each θ_n, the sinc function produces a null when its argument equals π. Following this observation, we can assume that the sum of N_θ sinc functions would produce a null when the sum of their arguments equals $N_\theta \pi$, approximately, i.e.,

$$\sum_n 2\pi N_l \Delta_l \sin \theta_n \sin \theta_u / \lambda = N_\theta \pi. \quad (15)$$

From (15), we can see that the first null occurs when

$$\sin \theta_u = \frac{N_\theta \lambda}{2L \sum_n \sin \theta_n} \quad (16)$$

and the AR then takes the form

$$\Delta_{\text{AR}}^{\text{FS−SAR}} = \frac{r_u N_\theta \lambda}{2L \sum_n \sin \theta_n}. \quad (17)$$

By comparing (12) and (16), we can understand the basic difference between the standard SAR and the FS-SAR approach. For an FL-SAR with an LA θ_n, the effective aperture is given by $L \sin \theta_u$, i.e., the aperture is decreased by an amount proportional to the LA. Whereas, for FS-SAR approach, the effective aperture is given by $L \sum_n \sin \theta_n / N_\theta$, the aperture is decreased by an amount proportional to the mean of the LAs. Thus, if the target is situated at the boresight of a very low LA, then, coherently adding its reflectivities with returns at slightly higher LAs, can basically increase the effective aperture. Fig. 4 shows the simulation results of FL-SAR antenna pattern at different LAs and the composite antenna pattern of FS-SAR approach. For FL-SAR, the beamwidth of antenna pattern increases with decreasing LA. However, the beamwidth of the antenna
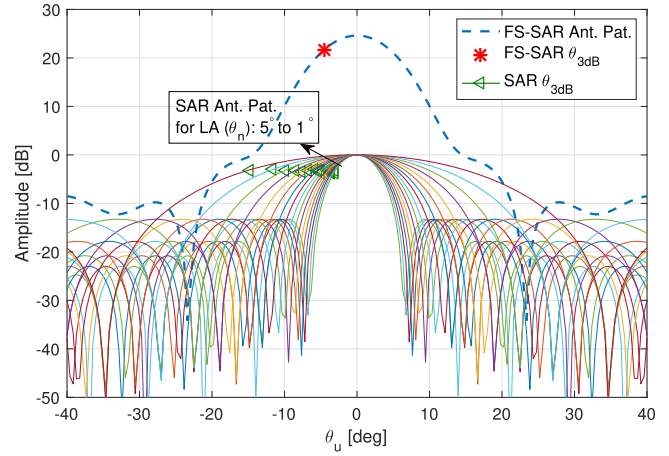
pattern with FS-SAR approach can be approximated with the mean of the beamwidths of the range of LAs. Fig. 4 also shows the approximate value of the first null for FS-SAR antenna pattern. Note that in Fig. 4, we have plotted a normalized version of the FS-SAR antenna pattern. The effect of FS-SAR approach is not only in terms of improvement in the effective aperture, but also in terms of an increase in the composite antenna gain. Fig. 5 shows the antenna patterns with actual values of the antenna gains. We can see that the FS-SAR approach exhibits higher antenna gains, which are proportional to the range of LAs. We also mark the $\theta_{3\,\text{dB}}$ points for all the cases. Here too, we can see that the 3 dB beamwidth of the FS-SAR approach can be approximated as the average of 3 dB beamwidths of FL-SAR at different LAs.

IV. FS-SAR ALGORITHMS

In this section, we provide two algorithms to implement FS-SAR methodology. Our approach is based on BP. Despite high computational requirements of BP, its flexibility for different SAR mode of operations makes it a feasible candidate for generating image of an Auto-radar. In this section, we also provide insights into reducing the computational complexity of our proposed algorithms.

A. Modified BP

We first introduce a modified version of BP. The basic principle of BP is to project all the measurements from each scanning step, on the aperture, back to the target location. Thus, measurements corresponding to the target location from all the scanning steps are coherently combined to generate a composite response of the synthetic aperture.[3] To this end, the measurements are upsampled via interpolation in order to correspond to a finer location grid in range, and subsequently integrated over the aperture to generate a SAR image. In our case, along with the range domain, we gain extra information from the angular

---

[3]Note, this is essentially a matched filtering operation in the aperture domain.

domain. Therefore, the interpolation can be done both in the range as well as in the azimuth. This phenomenon leads to the modification of the standard BP.

Let us represent $\mathbf{Y}_l$ from (10) in its upsampled form, by means of interpolation (in both range and azimuth) as, $\uparrow_{\kappa,\kappa} (\mathbf{Y}_l)$, where $\uparrow_{\kappa,\kappa'} (\cdot)$ denotes an upsampling function that interpolates a matrix by an order κ along its rows and by an order κ' along its columns.[4] Note, we assume $\kappa = \kappa'$, in our case.[5]

Given the target scene in CCS, the reconstructed image via modified BP (MBP) can be written as

$$\gamma_{ij}^{\text{MBP}} = \sum_{\theta} \sum_{l} [\uparrow_{\kappa,\kappa} (\mathbf{Y}_l)]_{\theta, I_{r_{ij}}} \qquad (18)$$

where $I_{r_{ij}}$ is the column index in $\uparrow_{\kappa,\kappa} (\mathbf{Y}_l)$ corresponding to range $r_{ij} = \sqrt{(x_i - l)^2 + y_j^2}$. Now, the following remarks regarding image reconstruction via MBP in (18) are in order.

1) The measurements are upsampled via interpolation over both the azimuth and the range domains.
2) Unlike traditional BP (where either the LA is fixed, i.e., for the case of Strip-SAR, or target range is fixed, i.e., for the case of Spot-SAR), the target information lies both in the range and the LAs, which is exploited by integrating over the aperture as well as over the angle.
3) Accumulation of backscattered energy over the angle and the aperture domains results in enhanced AR and better radar image reconstruction.

B. Compressed Sensing-Based BP

The FS-SAR method generates target information over both the aperture and the angular domains. Thus, the target response can be greatly increased. The MBP algorithm is essentially an MF operation in both the angle and the aperture domains. It has the ability of capturing all of the target backscattered energy. However, it is not efficient in creating stark contrast of reflectivity between neighboring scatterers. To this end, we use CS, so that the radar image should consist of very bright scatterers only, and the insignificant scatterers are suppressed. Our approach here is to use CS for each step on the aperture and then use standard BP to fulfil SAR processing.

Given the lth aperture step, we can apply CS over the azimuth for each range bin, or we can apply CS jointly for all the range bins within the maximum range at lth aperture step. In this paper, we choose the latter. In this manner, we can exploit target features for a wide range of scene targets. Let us rewrite (10) in the following vectorized form:

$$\mathbf{y}_l = \underbrace{[\mathbf{I}_{N_r} \otimes (\mathbf{GH})]}_{\triangleq \Phi} \mathbf{x}_l + \mathbf{n}_l \qquad (19)$$

where $\mathbf{y}_l \triangleq \text{vec}(\mathbf{Y}_l)$, $\mathbf{x}_l \triangleq \text{vec}(\mathbf{X}_l)$, and $\mathbf{n}_l \triangleq \text{vec}(\mathbf{N}_l)$ are $N_\theta N_r \times 1$, $N_x N_r \times 1$, and $N_\theta N_r \times 1$ vectors, respectively, and $\Phi \triangleq [\mathbf{I}_{N_r} \otimes (\mathbf{GH})]$ is an $N_\theta N_r \times N_x N_r$ joint measurement matrix. Since $N_\theta \ll N_x$, (19) is an underdetermined system of linear equations. Therefore, CS techniques can be helpful in finding an estimate of $\mathbf{x}_l$. This is generally done by solving the following optimization problem (OP):

$$\hat{\mathbf{x}}_l = \arg \min_{\mathbf{x}_l} \|\mathbf{y}_l - \Phi \mathbf{x}_l\|_2^2 + \lambda \|\mathbf{x}_l\|_1^1 \qquad (20)$$

where $\lambda > 0$. For (20), to provide a stable and unique solution, the CS framework puts certain conditions on the measurement matrix (i.e., Φ in our case), in order to guarantee the uniqueness and optimality of the sparse solution. One parameter of these conditions (which is easily verifiable as well) is known as mutual coherence (MC) [29]. MC is defined as the maximum absolute value of the inner product of different columns of the measurement matrix. It basically indicates the interdependence of the columns. In general, a lower value of MC can provide better results. Another parameter (which can be related to MC) is known as restricted isometry property (RIP) [30]. A measurement matrix (with unit normalized columns) is said to satisfy RIP of order K, given $\delta_K \in (0, 1)$, if

$$(1 - \delta_K) \leq \frac{\|\Phi \mathbf{x}_l\|_2^2}{\|\mathbf{x}_l\|_2^2} \leq (1 + \delta_K) \qquad (21)$$

where $K = \|\mathbf{x}_l\|_0^0$. In general terms, it means that the matrix Φ preserves Euclidean length of $\mathbf{x}_l$ and that every submatrix of Φ with less than K columns acts like an orthonormal matrix. The effect of these performance parameters generally boils down to a relationship between the number of measurements and the number of unknown nonzero elements to be estimated, i.e., K, for different measurement matrices, e.g., Gaussian, Bernoulli, and partial Fourier matrices [31]. A common characteristic of these measurement matrices is some form of randomness, which make sure that the elements in these matrices are spread out, i.e., their values are not concentrated on any specific location. In our case, the measurement matrix corresponds to the measurements taken at uniform angular interval Δ_θ. In order to conform to the conditions of MC and RIP, we can either 1) take measurements at completely random angular intervals, i.e., Δ_θ is a random variable, or 2) introduce jitter to the uniform sampling interval [32], i.e., the angular sampling interval becomes $\Delta_\theta + \vartheta_{n_\theta}$, where ϑ_{n_θ} is an independent random variable for, $n_\theta = 0, 1, \ldots, N_\theta - 1$. The choice between 1) and 2) depends on the possibility of their implementation in hardware. However, generally, angular samples are available for uniform intervals only. Some works, e.g., [23], provide heuristic assessments for using uniform angular samples to obtain reasonable performance results. In this paper, we continue with the measurements obtained at uniform angular intervals. However, it is clear that the availability of better measurement matrices would only provide even better results.

The OP in (20) is known as least absolute shrinkage and selection operator (LASSO) [33]. Its basic characteristic is

---

[4]Note, interpolation by an order κ, basically inserts $2^\kappa - 1$ sample points between the original samples, where the values of the newly interpolated sample points depend upon the type of interpolation used.

[5]Traditionally, an upsampling factor of $\kappa = 2$ can provide substantial gains.

to generate a sparse estimate of $\mathbf{x}_l$, where the order of sparsity is determined by the parameter λ. However, LASSO is devoid of exploiting any inherent structure in the elements of $\mathbf{x}_l$, other than element wise sparsity. A road scene, generally, consists of objects, e.g., cars, cycles, poles, etc., which have a continuum of a reflective surface. In this backdrop, it is better to use an OP which retrieves the correlations between consecutive elements of $\mathbf{x}_l$. To this end, we propose to use fused LASSO (F-LASSO) [34] for Auto-radar imaging. The F-LASSO OP can be written as

$$\hat{\mathbf{x}}_l = \arg \min_{\mathbf{x}_l} \|\mathbf{y}_l - \Phi \mathbf{x}_l\|_2^2 + \lambda \|\mathbf{x}_l\|_1^1 + \lambda_f \|\mathbf{D}\mathbf{x}_l\|_1^1 \quad (22)$$

where λ_f is a fusion penalty parameter (nonzero and positive) and $\mathbf{D}$ is the $N_x N_r \times N_x N_r$ fusion matrix, defined as

$$\mathbf{D} \triangleq \begin{pmatrix} -1 & +1 & 0 & 0 & \cdots & 0 & 0 \\ 0 & -1 & +1 & 0 & \cdots & 0 & 0 \\ \vdots & \vdots & \vdots & \vdots & \vdots & \vdots & \vdots \\ 0 & 0 & 0 & 0 & \cdots & -1 & +1 \\ 0 & 0 & 0 & 0 & \cdots & 0 & +1 \end{pmatrix} \quad (23)$$

with the result that $\|\mathbf{D}\mathbf{x}_l\|_1^1 = \sum_{m=1}^{N_x N_r - 1} \|[\mathbf{x}_l]_m - [\mathbf{x}_l]_{m-1}\|_1^1$, i.e., it relates to the difference of consecutive elements in $\mathbf{x}_l$. Thus, F-LASSO penalizes both the elements of $\mathbf{x}_l$ as well as their difference by an ℓ_1-norm. As a consequence, the reconstructed signal is parsimonious but also exhibits smooth transitions over its elements. This phenomenon leads to enhanced AR as well as an improved radar image.

The cost function in OP (22) is convex, in principle. However, for large-scale problems, iterative solvers are preferred. Since the cost function in (22) is neither continuously differentiable, nor separable in the elements of $\mathbf{x}_l$, we suggest to use an alternating direction method of multipliers [35], [36] based solver to estimate $\mathbf{x}_l$ (i.e., $\hat{\mathbf{x}}_l$) in (22). Now, let the estimate $\hat{\mathbf{x}}_l$ is reshaped into an $N_x \times N_r$ matrix $\hat{\mathbf{X}}_l$.[6] By using $\hat{\mathbf{X}}_l$, the radar image can be reconstructed via CS-based BP (CBP) as

$$\gamma_{ij}^{\text{CBP}} = \sum_l [\uparrow_{1,\kappa} (\hat{\mathbf{X}}_l)]_{I_{\theta_{ij}}, I_{r_{ij}}} \quad (24)$$

where $I_{\theta_{ij}}$ is the row index and $I_{r_{ij}}$ is the column index in $\uparrow_{1,\kappa} (\hat{\mathbf{X}}_l)$, corresponding to angle $\theta_{ij} = \arctan((x_i - l)/y_j)$ and range r_{ij}, respectively. Now, the following remarks regarding image reconstruction via CBP in (24) are in order.

1) Upsampling via interpolation is done in the range domain, whereas upsampling in the azimuth domain might be unnecessary since CS-based reconstruction provides ample upsampling itself.
2) Integration is done only over the aperture domain. Since CS-based reconstruction is in the angle domain, it provides better alternative to MF operation, resulting in sparse reconstruction.

3) By combining CS-based reconstruction over the angle domain with SAR processing, (24) guarantees enhanced AR and a better Auto-radar image.

C. Computational Complexity

Our proposed algorithms essentially build upon BP. Therefore, the computational complexity of our algorithms is primarily determined by the implementation of BP. A number of techniques have been proposed in the literature to reduce the computational complexity of BP, e.g., [37]–[39]. In this section, we explain how these techniques can be used in connection with our proposed algorithms to reduce the overall computational complexity.

Let the target scene is represented by an $N \times N$ pixel image/grid in CCS. Then, the computational complexity of BP is equivalent to collecting the total number of operations involved in finding the contribution of each image pixel in every measurement of the target scene. In this respect, the computational complexity of MBP can be written as

$$\mathcal{C}^{\text{MBP}} = \mathcal{O}(N_\theta N_l N^2) \quad (25)$$

where $\mathcal{O}(\cdot)$ denotes the order of complexity.[7] From (25), we can see that the major source of computation is to back project every measurement over the whole pixel grid. As pointed out in [37], if a subset of measurements (where the subset can be chosen based on the property of nearness among measurements) is back projected on a polar grid, we can reduce the frequency of mapping the measurements to the Cartesian grid. In our case, the angular measurements at a particular aperture position share a common point of reference. Therefore, we can back project all of the angular measurements on the polar grid, in principle, and then map the measurements to the Cartesian grid for a particular aperture position.

Similar ideas can be utilized to reduce the computational complexity over the aperture domain as well. The basic principle of all types of fast implementations of BP over the aperture domain is as follows: Partition the aperture into small subapertures, each subaperture corresponds to a coarse resolution so requires low computational complexity, combine all the subapertures into a final high resolution image. This aperture partitioning and combining can either be of a single level [37] or of multiple/hierarchical levels [38]. In the light of the above discussion, the computational complexity of our MBP algorithm can be generalized as

$$\mathcal{C}^{\text{MBP}} \approx \mathcal{O}(\log_b(N_l)N^2) \quad (26)$$

where $\log_b(N_l)$ is the number of hierarchical levels of the aperture in fast implementation of BP and b is the factorization basis.[8]

For CBP, the computational complexity over the aperture is the same as that of the MBP. However, in the angular domain, the computational complexity depends upon the

---

[6]Note, this is just a reverse operation of $\hat{\mathbf{x}}_l = \text{vec}(\hat{\mathbf{X}}_l)$.

[7]Note, here we have ignored the complexity of operations involved in upsampling/interpolation.
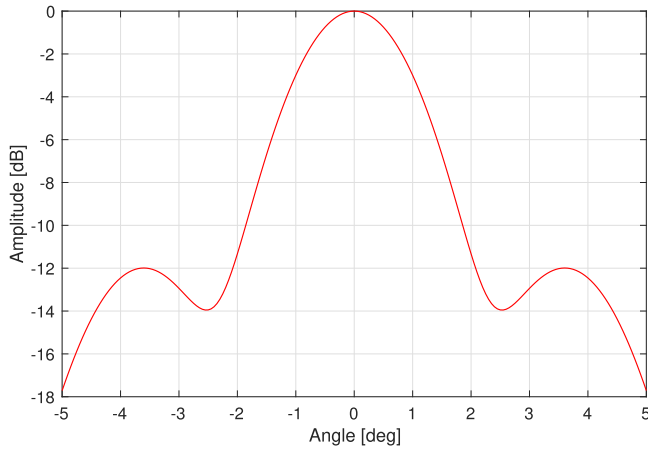[8]Note, $b = 3$ has been found to be the optimal factorization basis [40].

Fig. 6. Antenna pattern.

Fig. 7. Auto-radar measurement path.

reconstruction algorithm used to estimate $\mathbf{x}_l$. Most of the CS reconstruction algorithms have cubic or quadratic order of complexity. However, iterative approaches can have computational complexity lesser than quadratic. Nonetheless, CS-based reconstruction in CBP is carried out in the angle domain. Therefore, the reconstructed image is automatically defined on a polar grid. Thus, the computational complexity of CBP can generally be approximated to be similar to that of MBP, i.e., $\mathcal{C}^{\text{CBP}} \approx \mathcal{C}^{\text{MBP}}$.

V. EXPERIMENTAL VERIFICATION

In this section, we provide the experimental verification of our proposed algorithms and methodology via simulation as well as real-data experiments. We consider an FMCW monostatic radar operating at carrier frequency, $f_0 = 150$ GHz. We consider the radar signal bandwidth as, $B = 6$ GHz. Therefore, the range resolution can be calculated as $\Delta_r = 2.5$ cm.

A. Simulation

Following the radar specifications of [4], the 3 dB beamwidth of the horn antenna (for the considered radar) can be approximated as $\theta_{3\text{dB}} \approx 2°$. As is clear from Section II, knowledge of the exact beam pattern is essential for AR improvement, so we consider the beam pattern of a horn antenna as described by [41], which can be related to a mixture of Gaussian pdfs, i.e.,

$$h^2(\theta) = \sum_k a_k \exp((\theta - \mu_k)^2 / \sigma_\theta^2) \qquad (27)$$

where variance σ_θ^2 is set according to $\theta_{3\,\text{dB}}$, and coefficients a_k and positions μ_k are adjusted deterministically to emulate the beam pattern suggested by [41]. Fig. 6 shows such a beam pattern that has been used in our simulations. Notice the presence of sidelobes in the beam pattern. Their role can be crucial in determining the success of any AR enhancement methodology.

We consider the target scene as a grid, i.e., consisting of cells, in the CCS. A target may occupy a number of cells (i.e., an extended target). We consider the size of these cells equal to the range resolution in both axes. For the
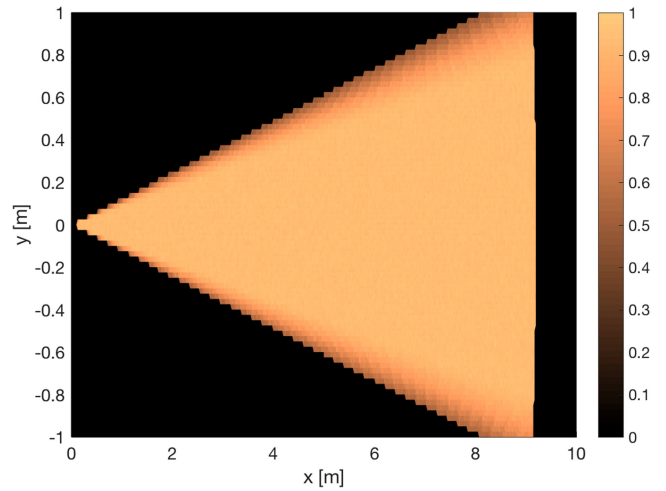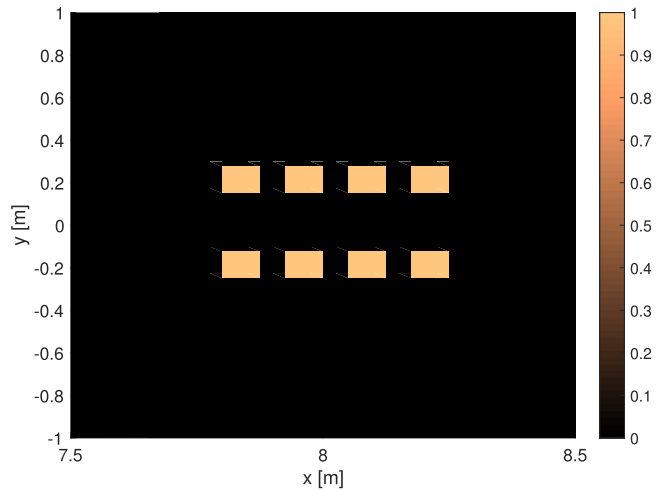

Fig. 8. Target scene in the CCS.

simulation, we assume the target scene to be an area of 2×10 m^2. The radar moves along the x-axis at $y = 0$. However, this movement pattern is just for the sake of presentation and does not limit the proposed methods. Fig. 7 shows the radar path. Over the aperture, we consider $N_l = 5$ aperture steps with the distance of $\Delta_l = 5$ cm between consecutive steps. Due to the FS-SAR methodology, the target area which is visited by radar more than other areas acquires higher backscattered energy. This can be seen in Fig. 7 by areas lit up with higher intensity. We consider $\theta_{\max} = 7°$. Therefore, the radar scans from $-7°$ to $+7°$, with angular steps, $\Delta_\theta = 0.2°$. Maximum range for each scan is limited to, $R_{\max} = 9$ m. We set up a target scene, which exhibits the nature of a typical road scene, i.e., consisting of extended targets. We consider eight target objects. Each target spans 5×3 group of cells. The distance between the objects along x-axis (which can be related to the range in our case), consists of two cells, i.e, 5 cm. The distance between the objects along y-axis (which can be related to the azimuth in our case), consists of ten cells, i.e., 25 cm. Fig. 8 shows the target scene. We generate measurements of the target scene according to (7). We assume AWGN for an SNR of
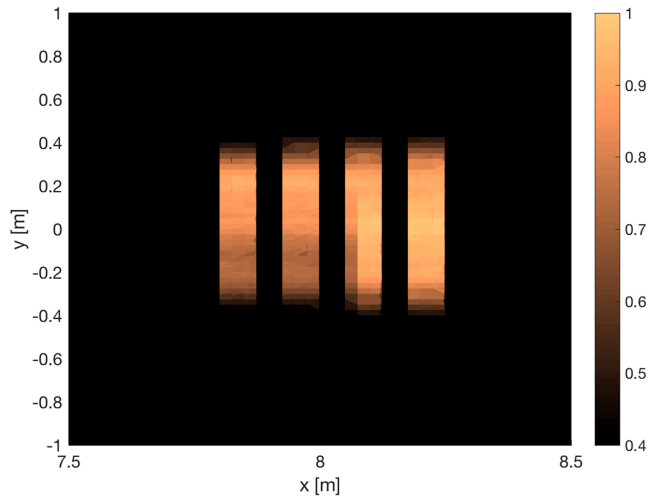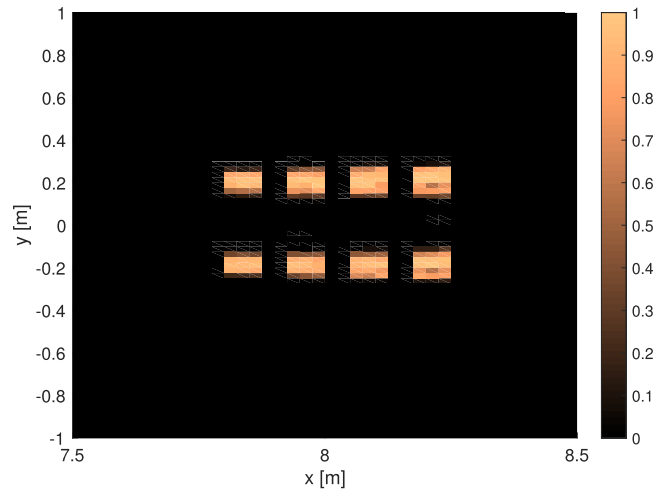
Fig. 9. Measured scene.

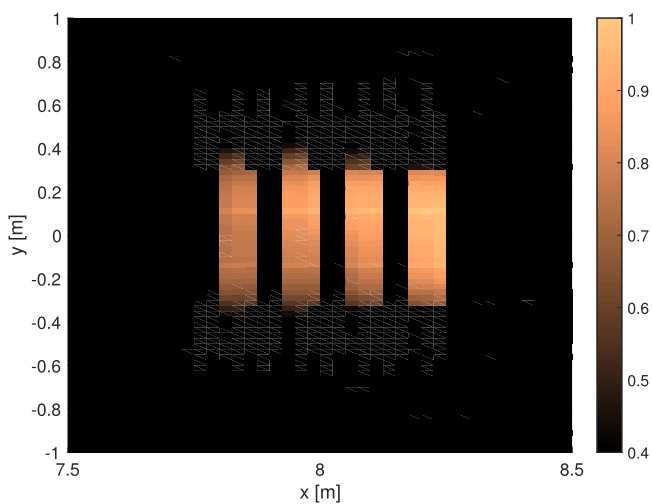

Fig. 11. Reconstructed image via CBP.
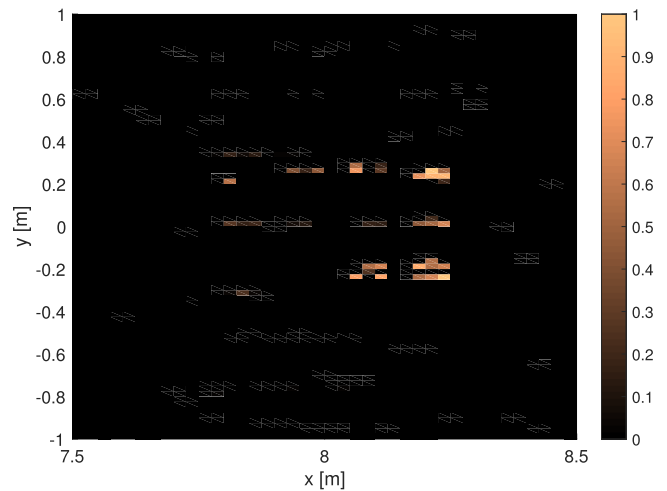

Fig. 10. Reconstructed image via MBP.

Fig. 12. Reconstructed image via OMP.

10 dB. The SNR is defined in terms of (19) as

$$\mathrm{SNR} \triangleq \frac{\|\boldsymbol{\Phi}\mathbf{x}_l\|_2^2}{N_\theta N_r \sigma^2}. \tag{28}$$

We generate measurements for every LA at every aperture step. However, we represent them collectively in Fig. 9, superimposed on each other. We can see that the objects are distinguishable in the range domain, primarily because of the fine range resolution of the radar. However, the azimuth domain cannot resolve the target objects.

Fig. 10 shows the result of reconstructing the image via MBP. In comparison to unprocessed measurements, the image constructed via MBP is better. The target objects in the azimuth domain are not strikingly apart. However, we can see a border distinguishing the objects. Fig. 11 shows the reconstructed image via CBP. We see better results than MBP. Each object has been reconstructed in its entirety. Target objects are clearly distinguishable both in the range as well as in the azimuth domain. The image is also free from any specular artefacts. Note that for CBP, we chose iterative solvers to estimate $\mathbf{x}_l$ in (22). The tuning parame-

ters λ and λ_f can be chosen via a cross validation procedure [42]. For the sake of comparison, we also construct the image with OMP. Note, OMP essentially solves an ℓ_0-norm (constrained) OP, instead of an ℓ_1-norm (unconstrained) OP in (20). Fig. 12 shows the reconstructed image. We can see that our proposed CBP approach performs much better than OMP. This is because of the inherent properties of the F-LASSO, i.e., to preserve target features as well as create parsimony in the solution.

B. Real Data

In this section, we apply our proposed algorithms on the real-data obtained via the FS-SAR methodology in controlled laboratory conditions, as an illustration. We consider two trolleys, separated by a certain distance, as our targets which is akin to two cars side-by-side. The size of a trolley equals (approx.) $1 \times 0.5 \times 0.55$ (length $\times$ width $\times$ height) m^3. We consider two values for separation, i.e., 15 and 5 cm. Fig. 13 shows the targets. It also shows a center line, which provides a trajectory of the radar movement, i.e., the radar moves along this line. We can see that the targets are offset from this center line. We consider an
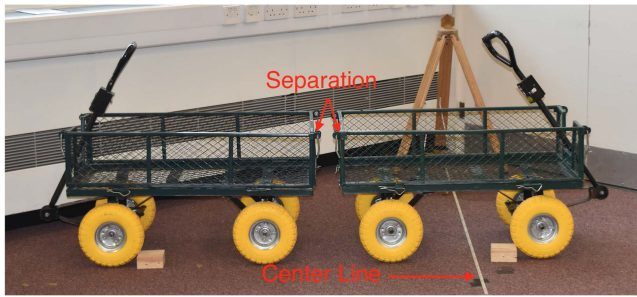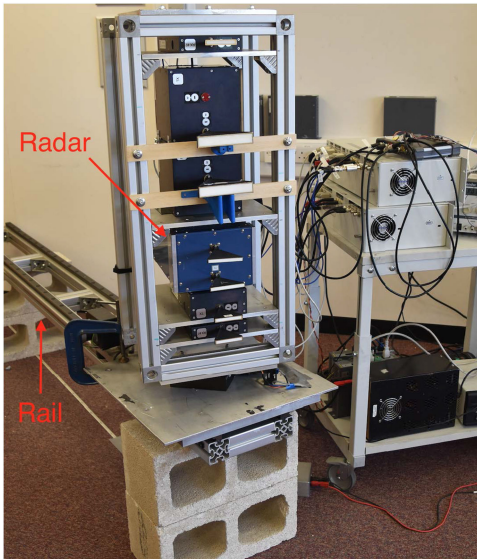
Fig. 13. Target scene.

Fig. 14. Radar and the rail.

Fig. 15. Real data measurement scenario.

Fig. 16. Measured antenna pattern.

offset angle of 5° from the centre of the synthetic aperture. In order to create a synthetic aperture, we use a rail, as shown in Fig. 14. The radar moves over this rail and scans the scene at different positions over the aperture. The length of the rail is $L = 1.8$ m and the distance of the target centre from the start of the center line is 8.6 m. We take aperture samples at 2.5 cm, with $N_l = 73$ samples in total. At each step on the aperture, the radar scans the target scene from $-10°$ to $+20°$ at angular steps $\Delta_\theta = 0.25°$. Fig. 15 provides a schematic of this scenario.

We first measured the antenna pattern of the radar since its accurate measurement is essential for the azimuth processing. Fig. 16 shows the measured antenna pattern with $\theta_{3\,dB} \approx 1.3°$. Note, Table I provides the complete specifications of the 150 GHz radar. Then, we took the scene measurements. Figs. 17 and 18 show the measured scenes when radar is closest to the targets over the aperture, for an intertarget separation of 15 and 5 cm, respectively. Note, we do not get any reflections from the middle walls of the trolleys. Therefore, the azimuth refinement concerns the recognition of corners of the trolley. We focus on the front corners of the trolleys facing each other, highlighted by a dotted ellipse. We can see from Figs. 17 and 18 that front corners are not distinguishable. Also, the radar image has missed
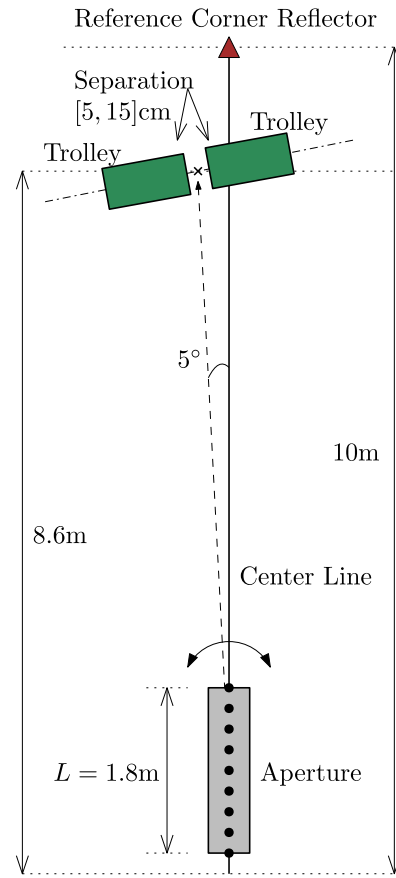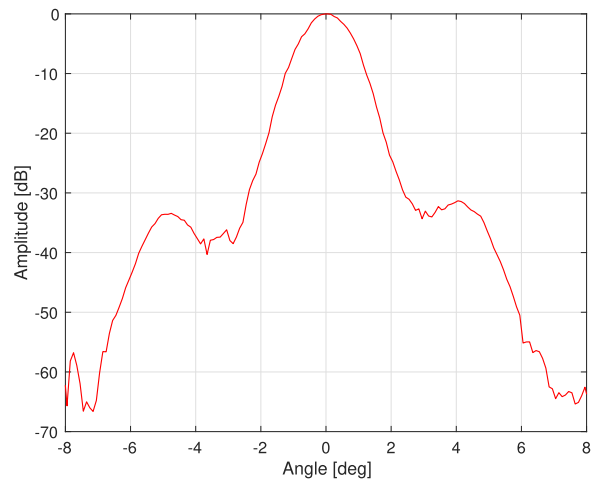
TABLE I
Specifications of 150 GHz Radar

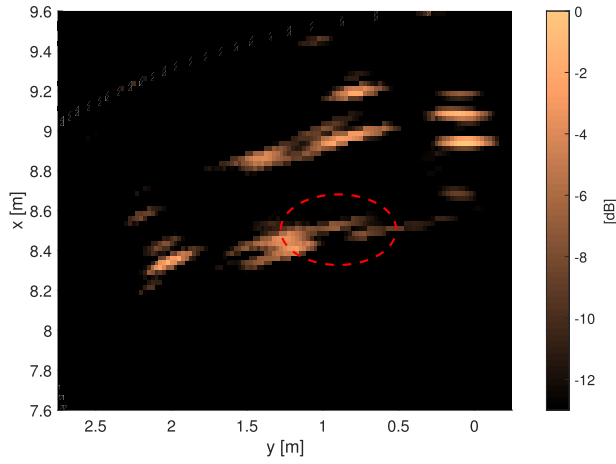| Modulation	FMCW
Frequency Range	$145 - 151$ GHz
Transmit Bandwidh (B)	6 GHz
Chirp Duration (T)	1.2 ms
Sampling Frequency	5 MHz
Angular Step (Δ_θ)	0.25°
Range Resolution (Δ_r)	0.025 m
3 dB Beamwidth ($\theta_{3\text{dB}}$)	1.3°

Fig. 17.   Measured scene: Closest to the targets at 15 cm separation.
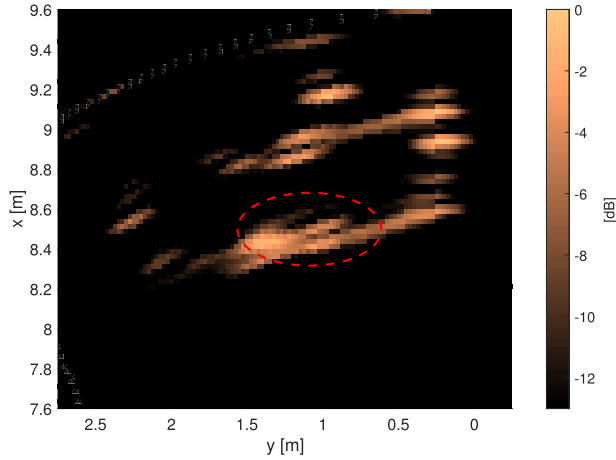

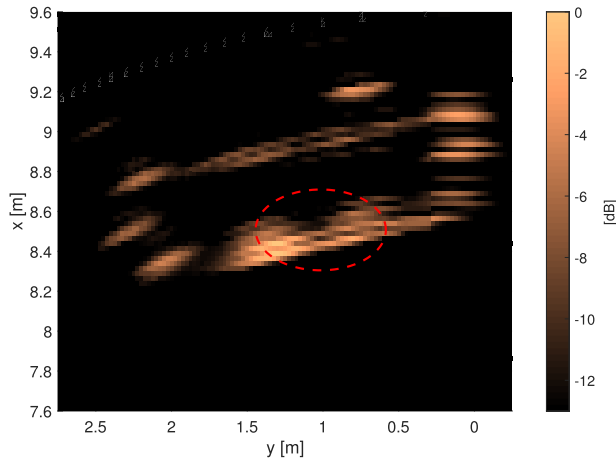Fig. 18.   Measured scene: Closest to the targets at 5 cm separation.

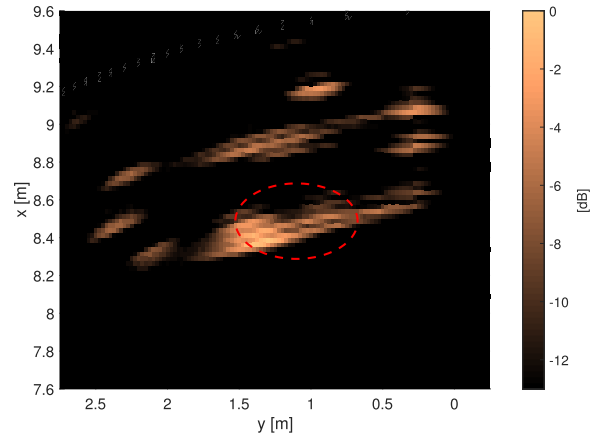Fig. 19.   Reconstructed image via MBP: 15 cm separation.

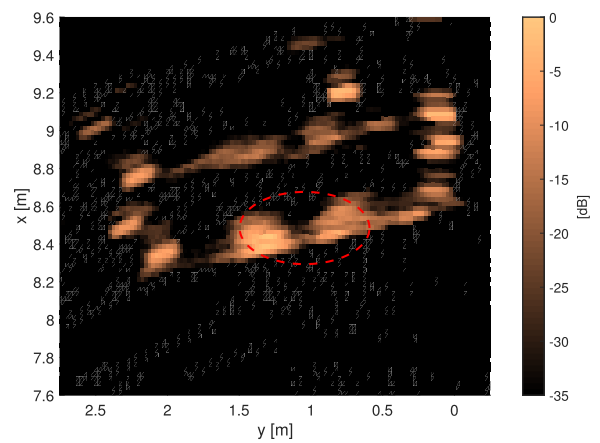Fig. 20.   Reconstructed image via MBP: 5 cm separation.

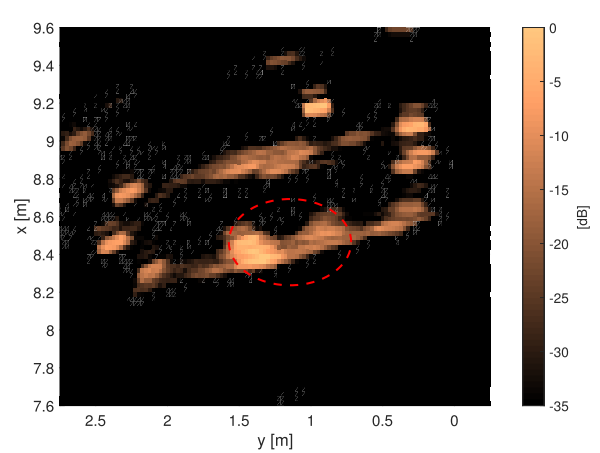Fig. 21.   Reconstructed image via CBP: 15 cm separation.

Fig. 22.   Reconstructed image via CBP: 5 cm separation.

substantial details of the trolley. In contrast, the image reconstructed via MBP as shown by Figs. 19 and 20 provides a better recognition of the corners of the trolleys, i.e., the separating grooves are better pronounced. Also, substantial details of the trolleys have been captured. Note, in our setting, the slant range from the aperture center to the center of targets is approximately 7 m. With $\theta_{3\,\mathrm{dB}} = 1.3°$, this amounts to AR of over 15 cm. From Fig. 20, we can

see that by using MBP, we have been able to enhance AR almost by a factor of 3. Figs. 21 and 22 show the results of reconstructing the image via CBP. We can see that the performance of CBP is even better than MBP. Thus, we can say that our proposed methods can provide significant gains to enhance AR and improve imaging of an FS-SAR.

Note, Figs. 19–22 essentially provide a qualitative analysis of the FS-SAR methodology. However, a quantitative
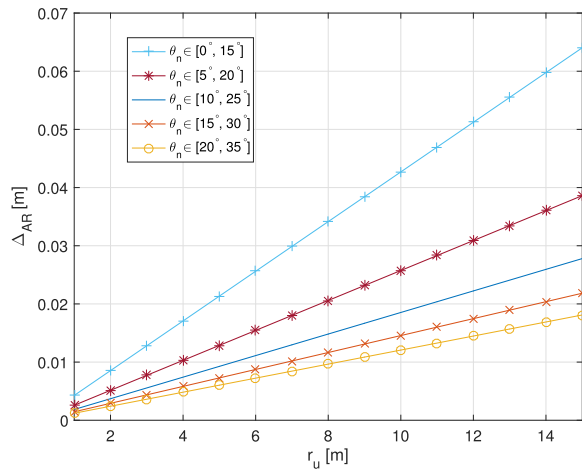
Fig. 23. Quantitative analysis of FS-SAR (17).

analysis of this methodology can be obtained by plotting (17) for different angular ranges of the scan. Fig. 23 provides such an analysis for varying ranges. Since our experimental set up falls in the angular range $\theta_n \in [0°, 15°]$, we can see that at a 10 m range, the AR of FS-SAR is (approx.) 4–5 cm, which is matched by the performance of our algorithms. Therefore, the performance of FS-SAR methodology is consistent both qualitatively as well quantitatively.

VI. CONCLUSION

In this paper, we have presented signal processing techniques to deliver Auto-radar imaging with improved AR. We have used FMCW signalling for a THz radar. We have proposed an FS-SAR methodology. We have shown that FS-SAR methodology causes an improvement in the effective aperture and an increase in the composite antenna gain. Thus, it results in the enhancement of AR. We have proposed two algorithms, namely, modified BP and CS-based BP, in order to capitalize on the gains of the FS-SAR technique. Both algorithms provide improved imaging. However, the latter has an edge over the former because it exploits the sparsity of the scene. The computational complexity of our proposed algorithms can also be easily managed. Results of simulation and real-data experiments prove the validity of our proposed methods. Future work consists of applying the proposed methods for imaging the moving targets in the presence of clutter.

REFERENCES

[1] K. Bengler, K. Dietmayer, B. Farber, M. Maurer, C. Stiller, and H. Winner
Three decades of driver assistance systems: Review and future perspectives
IEEE Intell. Transp. Syst. Mag., vol. 6, no. 4, pp. 6–22, Winter 2014.

[2] A. Eskandarian
Handbook of Intelligent Vehicles. New York, NY, USA: Springer-Verlag, 2012.

[3] E. Guizzo
How Google's self-driving car works
IEEE Spectrum Online, Oct. 2011. [Online]. Available: https://spectrum.ieee.org/automaton/robotics/artificial-intelligence/how-google-self-driving-car-works

[4] D. Jasteh, E. G. Hoare, M. Cherniakov, and M. Gashinova
Experimental low-terahertz radar image analysis for automotive terrain sensing
IEEE Geosci. Remote Sens. Lett., vol. 13, no. 4, pp. 490–494, Apr. 2016.

[5] M. Murad *et al.*
Requirements for next generation automotive radars
In *Proc. IEEE Radar Conf.*, Apr. 2013, pp. 1–6.

[6] S. M. Patole, M. Torlak, D. Wang, and M. Ali
Automotive radars: A review of signal processing techniques
IEEE Signal Process. Mag., vol. 34, no. 2, pp. 22–35, Mar. 2017.

[7] G. Krieger *et al.*
Sector imaging radar for enhanced vision
Aerosp. Sci. Technol., vol. 7, no. 2, pp. 147–158, 2003.

[8] A. Farina, F. Gini, and M. Greco
DOA estimation by exploiting the amplitude modulation induced by antenna scanning
IEEE Trans. Aerosp. Electron. Syst., vol. 38, no. 4, pp. 1276–1286, Oct. 2002.

[9] G. Liu, K. Yang, B. Sykora, and I. Salha
Range and azimuth resolution enhancement for 94 GHz real-beam radar
In *Proc. SPIE Radar Sens. Technol. XII*, 2008, vol. 6947, pp. 1–9.

[10] S. Uttam and N. A. Goodman
Superresolution of coherent sources in real-beam data
IEEE Trans. Aerosp. Electron. Syst., vol. 46, no. 3, pp. 1557–1566, Jul. 2010.

[11] M. A. Richards
Fundamentals of Radar Signal Processing. New York, NY, USA: McGraw-Hill, 2005.

[12] M. A. Richards
Iterative noncoherent angular superresolution [radar]
In *Proc. IEEE Nat. Radar Conf.*, Apr. 1988, pp. 100–105.

[13] S. D. Blunt and K. Gerlach
Adaptive pulse compression via MMSE estimation
IEEE Trans. Aerosp. Electron. Syst., vol. 42, no. 2, pp. 572–584, Apr. 2006.

[14] M. Ruggiano, E. Stolp, and P. van Genderen
Improvement of target resolution in azimuth by LMMSE technique
In *Proc. Eur. Radar Conf.*, Sep. 2009, pp. 230–233.

[15] J. Guan, J. Yang, Y. Huang, and W. Li
Maximum a posteriori based angular superresolution for scanning radar imaging
IEEE Trans. Aerosp. Electron. Syst., vol. 50, no. 3, pp. 2389–2398, Jul. 2014.

[16] F. Lenti, F. Nunziata, M. Migliaccio, and G. Rodriguez
Two-dimensional TSVD to enhance the spatial resolution of radiometer data
IEEE Trans. Geosci. Remote Sens., vol. 52, no. 5, pp. 2450–2458, May 2014.

[17] Y. Huang, Y. Zha, Y. Wang, and J. Yang
Forward looking radar imaging by truncated singular value decomposition and its application for adverse weather aircraft landing
Sensors, vol. 15, no. 6, pp. 14 397–14 414, 2015.

[18] D. L. Donoho
Compressed sensing
IEEE Trans. Inf. Theory, vol. 52, no. 4, pp. 1289–1306, Apr. 2006.

[19] E. Candes, J. Romberg, and T. Tao
Robust uncertainty principles: exact signal reconstruction from highly incomplete frequency information
IEEE Trans. Inf. Theory, vol. 52, no. 2, pp. 489–509, Feb. 2006.

[20] L. C. Potter, E. Ertin, J. T. Parker, and M. Cetin
Sparsity and compressed sensing in radar imaging
Proc. IEEE, vol. 98, no. 6, pp. 1006–1020, Jun. 2010.

[21] M. A. Herman and T. Strohmer
High-resolution radar via compressed sensing
IEEE Trans. Signal Process., vol. 57, no. 6, pp. 2275–2284, Jun. 2009.

[22] S. I. Kelly, G. Rilling, M. Davies, and B. Mulgrew
Iterative image formation using fast (re/back)-projection for spotlight-mode SAR
In *Proc. IEEE Radar Conf.*, May 2011, pp. 835–840.

[23] X. Wen, G. Kuang, J. Hu, R. Zhan, and J. Zhang
Forward-looking imaging of scanning phased array radar based on the compressed sensing
Prog. Electromagn. Res., vol. 143, pp. 575–604, 2013.

[24] M. Soumekh
Synthetic Aperture Radar. Hoboken, NJ, USA: John Wiley & Sons, 1999.

[25] A. Meta, P. Hoogeboom, and L. P. Ligthart
Signal processing for FMCW SAR
IEEE Trans. Geosci. Remote Sens., vol. 45, no. 11, pp. 3519–3532, Nov. 2007.

[26] R. Wang, O. Loffeld, H. Nies, S. Knedlik, M. Hagelen, and H. Essen
Focus FMCW SAR data using the wavenumber domain algorithm
IEEE Trans. Geosci. Remote Sens., vol. 48, no. 4, pp. 2109–2118, Apr. 2010.

[27] A. Ribalta
Time-domain reconstruction algorithms for FMCW-SAR
IEEE Geosci. Remote Sens. Lett., vol. 8, no. 3, pp. 396–400, May 2011.

[28] W. Carrara, R. Goodman, and R. Majewski
Spotlight Synthetic Aperture Radar. Boston, MA, USA: Artech House, 1995.

[29] D. L. Donoho and M. Elad
Optimally sparse representation in general (non-orthogonal) dictionaries via ℓ_1 minimization
Proc. Nat. Acad. Sci.United States Amer., vol. 100, no. 5, pp. 2197–2202, Mar. 2003.

[30] E. Candes and T. Tao
Decoding by linear programming
IEEE Trans. Inf. Theory, vol. 51, no. 12, pp. 4203–4215, Dec. 2005.

[31] E. Candes and M. Wakin
An introduction to compressive sampling
IEEE Signal Process. Mag., vol. 25, no. 2, pp. 21–30, Mar. 2008.

[32] G. Hennenfent and F. J. Herrmann
Simply denoise: Wavefield reconstruction via jittered under-sampling
GEOPHYSICS, vol. 73, no. 3, pp. V19–V28, 2008.

[33] R. Tibshirani
Regression shrinkage and selection via the LASSO
J. Royal Statist. Soc., Series B, vol. 58, pp. 267–288, 1994.

[34] R. Tibshirani, M. Saunders, S. Rosset, J. Zhu, and K. Knight
Sparsity and smoothness via the fused LASSO
J. Royal Statist. Soc. Series B, vol. 67, pp. 91–108, 2005.

[35] D. P. Bertsekas and J. N. Tsitsiklis.
Parallel and Distributed Computation: Numerical Methods. Cambridge, MA, USA: MIT Press, 1997.

[36] S. Gishkori and G. Leus
Compressed sensing for block-sparse smooth signals
In *Proc. IEEE Int. Conf. Acoust., Speech Signal Process.*, May 2014, pp. 4166–4170.

[37] A. F. Yegulalp
Fast backprojection algorithm for synthetic aperture radar
In *Proc. IEEE Radar Conf. Radar Next Millennium*, 1999, pp. 60–65.

[38] L. M. H. Ulander, H. Hellsten, and G. Stenstrom
Synthetic-aperture radar processing using fast factorized back-projection
IEEE Trans. Aerosp. Electron. Syst., vol. 39, no. 3, pp. 760–776, Jul. 2003.

[39] P. O. Frolind and L. M. H. Ulander
Evaluation of angular interpolation kernels in fast back-projection SAR processing
IEE Proc.—Radar, Sonar Navigat., vol. 153, no. 3, pp. 243–249, Jun. 2006.

[40] A. Ribalta
Optimizing the factorisation parameters in the fast factorized backprojection algorithm
In *Proc. 9th Eur. Conf. Synthetic Aperture Radar*, Apr. 2012, pp. 356–359.

[41] M. Teichman
Determination of horn antenna phase centers by edge diffraction theory
IEEE Trans. Aerosp. Electron. Syst., vol. AES-9, no. 6, pp. 875–882, Nov. 1973.

[42] B. Efron and R. J. Tibshirani
An Introduction to the Bootstrap. New York, NY, USA: Chapman & Hall, 1993.

Shahzad Gishkori received the B.Sc. degree in electrical engineering from the University of Engineering and Technology Lahore, Lahore, Pakistan, in 2002, and the M.Sc. (cum Laude) and Ph.D. degrees in electrical engineering from the Delft University of Technology, Delft, The Netherlands, in 2009 and 2014, respectively.

From 2014 to 2015, he was a Postdoctoral Research Associate with Imperial College London, London, U.K. Since February 2016, he has been working as a Postdoctoral Research Associate with the University of Edinburgh, Edinburgh, U.K. His research interests include compressed sensing, signal processing, and wireless communications.

Liam Daniel received the M.Sc. degree in theoretical physics in 2005 and the Ph.D. degree in maritime forward scatter radar development in 2017, both from the University of Birmingham, Birmingham, U.K.

He is currently a Research Fellow at the Microwave Integrated Systems Laboratory, School of Engineering, University of Birmingham, Birmingham, U.K. His research interests include experimental, theoretical, simulation and signal processing aspects of bistatic radars with a focus on forward scatter radar and passive sensing, automotive sensing, and low-THz radar systems.

Marina Gashinova received the M.Math degree from St.-Petersburg State University, Saint Peterburg, Russia, in 1991, and the Ph.D. degree in physics and mathematics from St.-Petersburg Electrotechnical University, Saint Petersburg, Russia, in 2003.

In 2006, she joined the Microwave Integrated System Laboratory, University of Birmingham, Birmingham, U.K., as a Research Fellow. She is currently a Professor of Radar and RF Sensors, leading the research group on passive and active bistatic radar, THz multi-feature imaging radar, and automotive sensors.

Bernard Mulgrew (F'12) received the B.Sc. degree from Queen's University Belfast, Belfast, U.K., in 1979, and the Ph.D. degree from University of Edinburgh, Edinburgh, U.K., in 1987.

After graduation, he worked for 4 years as a Development Engineer with the Radar Systems Department, Ferranti, Edinburgh. From 1983 to 1986, he was a Research Associate with the Department of Electrical Engineering, University of Edinburgh, Edinburgh, U.K. He was appointed as a Lecturer in 1986, promoted to a Senior Lecturer in 1994 and became a Reader in 1996. The University of Edinburgh appointed him to a Personal Chair in October 1999 (Professor of Signals and Systems). He has co-authored three books on signal processing. His research interests include adaptive signal processing and estimation theory and in their application to radar and sensor systems.

Dr. Mulgrew is a Fellow of the Royal Academy of Engineering, Royal Society of Edinburgh, and IET.